

Title

Matthew Lawrence Joyce

October 9, 2020

CONTENTS

1.	<i>The Standard Model</i>	5
2.	<i>Supersymmetry</i>	6
3.	<i>The Large Hadron Collider</i>	7
3.1	Introduction	7
3.2	Injection Complex	7
3.3	Tunnel and Magnets	8
3.4	Luminosity	10
4.	<i>Compact Muon Solenoid</i>	12
4.1	Introduction	12
4.2	Coordinate System	13
4.3	Superconducting Magnet	14
4.4	Tracker	14
4.4.1	Pixel Detector	14
4.4.2	Strip Detector	15
4.5	Electromagnetic Calorimeter	16
4.5.1	Crystals	17
4.5.2	Barrel and Endcaps	18
4.5.3	Preshower layer	19
4.5.4	Performance	19
4.6	Hadronic Calorimeter	20
4.7	Muon System	20
5.	<i>MIP Timing Detector (MTD)</i>	21
5.1	Introduction	21
5.2	Barrel Timing Layer	22

LIST OF FIGURES

3.1	LHC interaction points	8
3.2	Layout of LHC accelerator complex [9].	9
3.3	Proton bunch capture onto RF bucket [2].	10
3.4	Cross section of LHC dipole [4]	11
3.5	Integrated luminosity delivered by the LHC to the CMS experiment each year from 2010-2018.	11
4.1	Schematic of CMS detector [10]	12
4.2	Transverse slice of the CMS detector[3].	13
4.3	Cross section (side) of CMS tracker prior to the Phase 1 upgrade during the year-end technical stop of 2016/2017. Each line represents a detector module while double lines indicate back-to-back strip modules. Surrounding the pixel tracker (PIXEL) is the strip detector, which is divided into the Tracker Inner Barrel (TIB), Tracker Outer Barrel (TOB), Tracker Inner Disks (TID), and Tracker Endcaps (TEC). Reprinted from Reference [6].	15
4.4	Cross section (side) of pixel detector. The lower half , labeled "Current", shows the design prior to 2017 while the upper half, labeled "Upgrade", shows the design after the upgrade. Reprinted from Resource [5]	16
4.5	PbWO ₄ crystals. Left: EB crystal with APD. Right: EE crystal with VPT. Reprinted from [7]	18
4.6	Schematic of ECAL. Reprint from [7]	19
4.7	Longitudinal view of HCAL	20
5.1	Timeline for LHC	21
5.2	Vertices from a simulated 200 pileup event. Need to replace this with the figure from the TDR.	22

LIST OF TABLES

4.1 Summary of signals expected for each particle type in each sub-detector.	13
-----------------------------------------------------------------------------------------	----

1. THE STANDARD MODEL

2. SUPERSYMMETRY

3 3. THE LARGE HADRON COLLIDER

4 3.1 *Introduction*

5 The Large Hadron Collider (LHC) is a 26.7 kilometer-long, two-ring particle
6 accelerator and collider located on the border of France and Switzerland at
7 the European Organization for Nuclear Research (CERN). During normal
8 operations the LHC maintains two counter-rotating beams of proton bunches
9 that collide at four interaction points (IP) with up to $\sqrt{s} = 14$ TeV center
10 of mass energy and a luminosity of $10^{34}\text{cm}^{-2}\text{s}^{-1}$. The ALICE (Point 2),
11 ATLAS (Point 1), CMS (Point 5), and LHC-b experiments each have a
12 detector at one of these interaction points as scene in Figure 3.1 . The CMS
13 and ATLAS are general-purpose detectors while LHC-b specializes in beauty
14 quark studies. ALICE is a heavy-ion experiment which uses $^{208}\text{Pb} - p$ or
15 $^{208}\text{Pb} - ^{208}\text{Pb}$ collisions that can also be produced by the LHC.

16 3.2 *Injection Complex*

17 In order to bring the protons from rest up to their target collision energy
18 a series of accelerators, as shown in Figure 3.2, are used. The acceleration
19 sequence begins with the injection of hydrogen gas into a duoplasmatron.
20 Here a bombardment of electrons ionize the hydrogen atoms while an electric
21 field pushes them through the duoplasmatron cavity. The result is 100 keV
22 protons being passed on to a quadrupole magnet which guides them into
23 the aperture of a linear accelerator (LINAC2). The radio frequency (RF)
24 cavities in LINAC2 accelerate the protons up to 50 MeV. At this point the
25 protons are sent into one of four rings in the Proton Synchrotron Booster
26 (PSB). The PSB repeatedly accelerates the protons around a circular path
27 until they reach an energy of 1.4 GeV. The bunches of protons from each PSB
28 ring are then sequentially injected into the single-ringed Proton Synchrotron
29 (PS). Each bunch injected into the PS are captured by one of the "buckets"
30 (Figure 3.3) provided by the PS RF system which also manipulates the
31 bunches into the desired profile and proton density. These proton bunches
32 are accelerated to 25 GeV and injected into the Super Proton Synchrotron

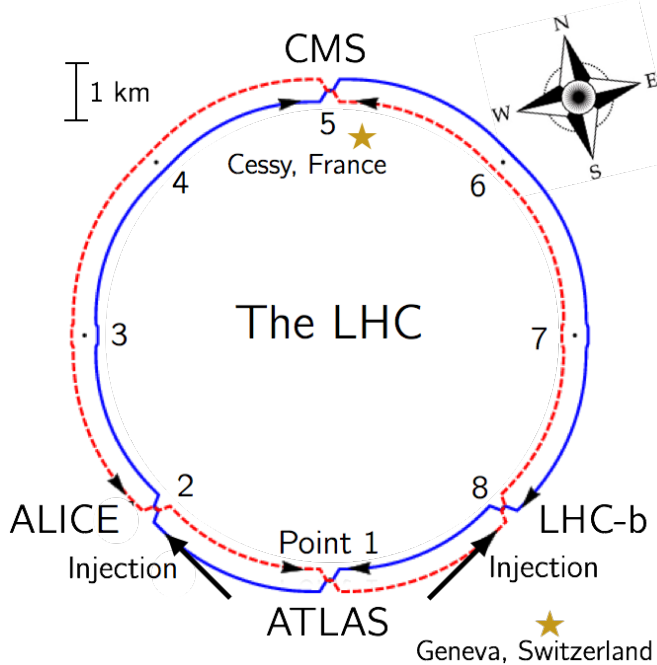


Fig. 3.1: Interaction points of the LHC

³³ (SPS) where they are accelerated to 450 GeV. Finally the proton bunches
³⁴ are injected into the LHC ring where they are accelerated to 6.5 TeV and
³⁵ collided in 25 ns intervals to yield a center of mass energy of $\sqrt{s} = 13$ TeV.

³⁶ 3.3 Tunnel and Magnets

³⁷ The LHC was designed to produce collisions with up to $\sqrt{s} = 14$ TeV. That
³⁸ requires confining and guiding 7 TeV protons around the circumference of
³⁹ the LHC ring. The ring is housed in a 4 meter-wide underground tunnel
⁴⁰ that ranges in depth between 45 and 170 meters below the surface. This
⁴¹ tunnel was repurposed from the Large Electron-Positron (LEP) Collider
⁴² which previously occupied the space. For this reason the tunnel is not
⁴³ completely circular but is instead made up of alternating curved and straight
⁴⁴ sections of 2500 m and 530 m in length respectively. The straight sections,
⁴⁵ labeled 1-8 in Figure 3.1, are used as either experimental facilities or sites for
⁴⁶ hardware necessary for LHC operations such as RF cavities for momentum
⁴⁷ cleaning, quadrupole magnets for beam focusing, and sextupole magnets for
⁴⁸ acceleration and betatron cleaning.

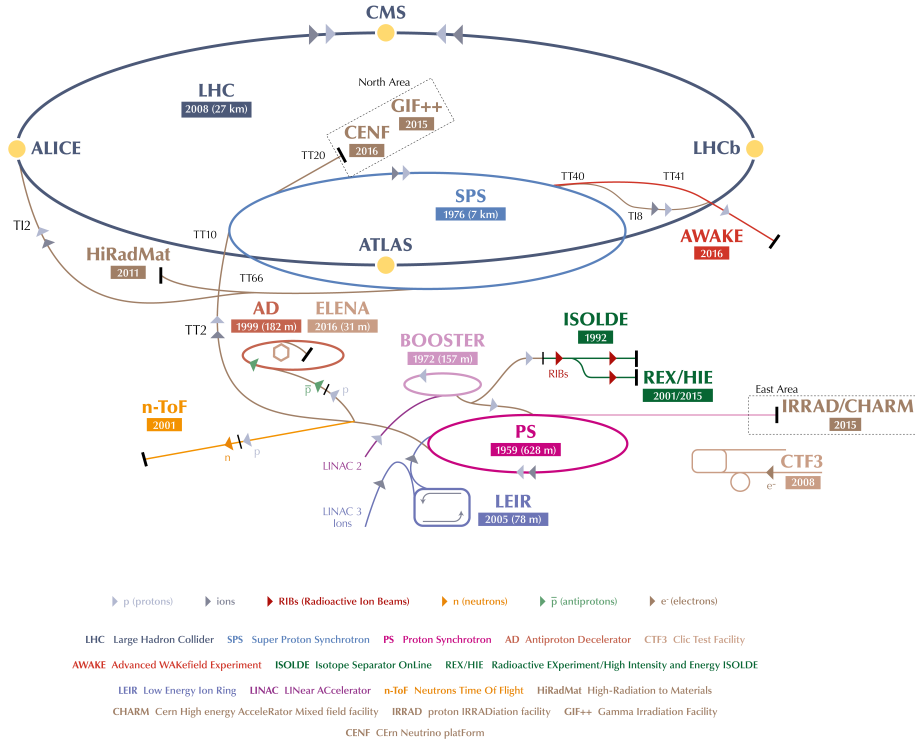


Fig. 3.2: Layout of LHC accelerator complex [9].

49 Steering a 7 TeV proton beam around the curved sections requires a mag-
50 netic field of 8.33 Tesla which is provided by 1223 superconducting dipole
51 magnets cooled to 1.9 K. A cross section of the LHC dipole is shown in
52 Figure 3.4. Supercooled liquid helium flows through the heat exchanger
53 pipe to cool the iron yolk to a temperature of 1.9 K. Ultra high vacuum
54 is maintained in the outer volume to provide a layer of thermal insulation
55 between the inner volume and the outer steel casing. Inside the iron yolk is a
56 twin bore assembly of niobium-titanium superconducting coils. Two parallel
57 beam pipes are located within the focus of the superconducting coils. This
58 is the ultra high vacuum region where the subatomic particles are confined
59 as they travel around the LHC ring.

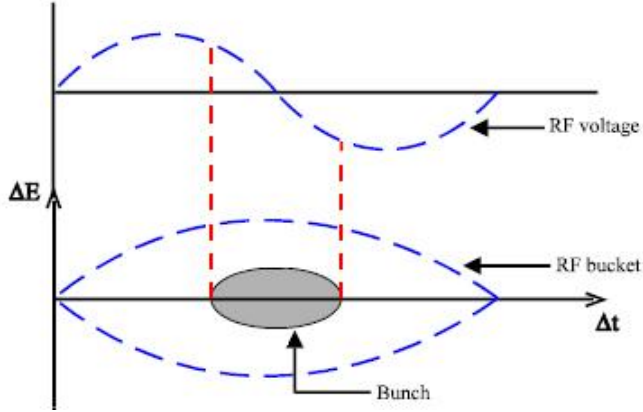


Fig. 3.3: Proton bunch capture onto RF bucket [2].

3.4 Luminosity

61 The number of events generated per second for specific process having cross-
62 section σ_{event} is given by:

$$\frac{dN_{event}}{dt} = L\sigma_{event} \quad (3.1)$$

63 where L is the machine luminosity. The machine luminosity for a Gaussian
64 beam distribution can be written in terms of the beam parameters as:

$$L = \frac{N_b^2 n_b f_{rev} \gamma_r}{4\pi \epsilon_n \beta_*} F \quad (3.2)$$

65 where N_b is particle density in each bunch, n_b is the number of bunches
66 in each beam, f_{rev} is the frequency of revolution, and γ_r is the relativistic
67 gamma factor. The variables ϵ_n and β_* are the normalized transverse beam
68 emittance and the beta function at the IP respectively, while F is the geo-
69 metric reduction factor depending due to the beams' crossing angle at the
70 IP. [9]

71 The total number of events produced over a given amount of time would
72 then be

$$N_{event} = \sigma_{event} \int L dt = \sigma_{event} L_{integrated}. \quad (3.3)$$

73 The integrated luminosity delivered each year to the CMS experiment is
74 shown in 3.5. The analysis presented here uses data collected from the 2016,
75 2017, and 2018 campaigns which gives a combined integrated luminosity of
76 158.7 fb^{-1} .

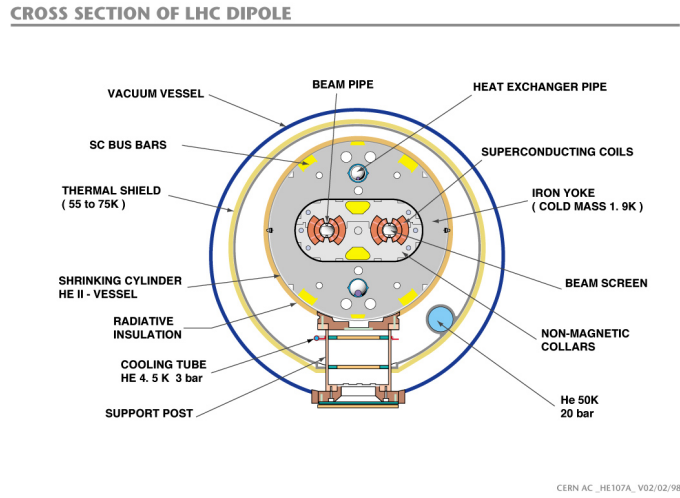


Fig. 3.4: Cross section of LHC dipole [4]

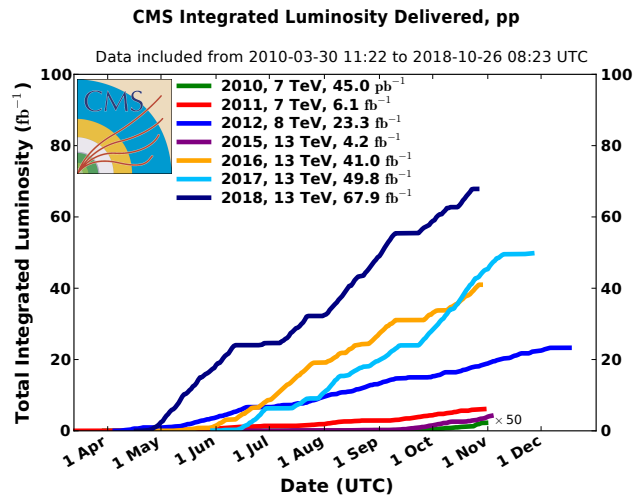


Fig. 3.5: Integrated luminosity delivered by the LHC to the CMS experiment each year from 2010-2018.

4. COMPACT MUON SOLENOID

4.1 Introduction

79 About 100 meters below the town of Cessy, France at Point 5 is the Compact
 80 Muon Solenoid (CMS). The CMS is a general purpose detector weighing
 81 14,000 tonnes with a length of 28.7 meters and a 15.0-meter diameter that
 82 was designed to accurately measure the energy and momentum of particles
 83 produced in the proton-proton or heavy-ion collisions at the LHC [7]. A
 84 perspective view of the detector is shown in Figure 4.1. In order to get
 85 a full picture of what is being produced by the collisions the CMS detector
 86 must be able identify the resulting particles as well as accurately measure
 87 their energy and momentum. For this reason the detector was designed to
 88 be a collection of specialized sub-detectors, each of which contributes data
 used in the reconstruction of a collision.

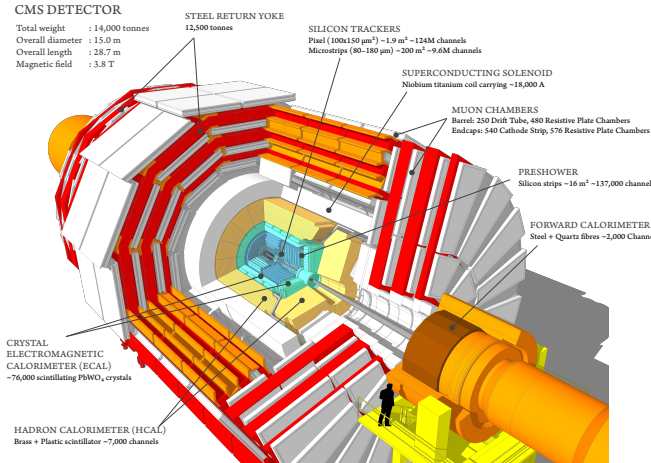


Fig. 4.1: Schematic of CMS detector [10]

90 At the heart of the CMS detector is a 3.8-Tesla magnetic field produced
 91 by a superconducting solenoid. Inside the 6-meter diameter solenoid are

92 three layers of sub-detectors. These make up the inner detector and are, in
 93 order from innermost to outermost, the silicon tracker, the electromagnetic
 94 calorimeter (ECAL), and the hadronic calorimeter (HCAL). Outside the
 95 solenoid is the muon system. A transverse slice of the detector (Figure 4.2)
 96 shows the sub-detectors and how different types of particles interact with
 97 with them. Table 4.1 shows a summary of which sub-detectors are expected
 98 to produce signals for different types of particles.

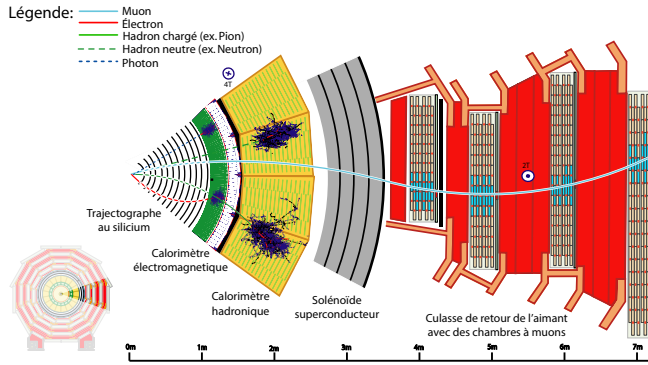


Fig. 4.2: Transverse slice of the CMS detector[3].

Particle	Tracker	ECAL	HCAL	Muon
Photons	No	Yes	No	No
Electrons	Yes	Yes	No	No
Hadrons (charged)	Yes	Yes	Yes	No
Hadrons (neutral)	No	No	Yes	No
Muons	Yes	No	No	Yes
Invisible (ν , SUSY, etc)	No	No	No	No

Tab. 4.1: Summary of signals expected for each particle type in each sub-detector.

4.2 Coordinate System

99
 100 The origin of the coordinate system used by CMS is centered at the nominal
 101 collision point in the center of the detector. A right-handed Cartesian system
 102 is used with the x-axis pointing radially inward toward the center of the LHC
 103 ring, y-axis pointing vertically upward, and the z-axis pointing tangent to

104 the LHC ring in the counterclockwise direction as viewed from above. CMS
 105 also uses an approximately Lorentz invariant spherical coordinate system
 106 spanned by three basis vectors. They are the transverse momentum p_T ,
 107 pseudorapidity η , and azimuthal angle ϕ . The transverse momentum and
 108 azimuthal angle translate to the Cartesian system in the following ways
 109 using the x and y-components of the linear momentum:

$$p_T = \sqrt{(p_x)^2 + (p_y)^2} \quad (4.1)$$

110

$$\phi = \tan^{-1} \frac{p_y}{p_x} \quad (4.2)$$

111 while the pseudorapidity can be translated using the polar angle θ relative
 112 the positive z-axis as

$$\eta = -\ln[\tan \frac{\theta}{2}]. \quad (4.3)$$

113 4.3 Superconducting Magnet

114 4.4 Tracker

115 The innermost sub-detector in CMS is the silicon tracker. The tracker is
 116 used to reconstruct tracks and vertices of charged particles. In order to give
 117 precise reconstruction of charged particle trajectories it needs to be position
 118 as close as possible to the IP and have high granularity. The close proximity
 119 to the IP requires the materials to be tolerant to the high levels of radiation
 120 in that region. Being the innermost sub-detector it must also minimally
 121 disturb particles as they pass through it into the other sub-detectors. These
 122 criteria led to the design of the tracker using silicon semiconductors.

123 The silicon tracker is made up of two subsystems, an inner pixel detector
 124 and an outer strip tracker which are oriented in a cylindrical shape with an
 125 overall diameter of 2.4 m and length of 5.6 m centered on the interaction
 126 point. Both subsystems consist of barrel and endcap regions which can be
 127 seen in Figure 4.3.

128 4.4.1 Pixel Detector

129 The pixel detector is the innermost subsystem in the silicon tracker and
 130 spans the pseudorapidity range $|\eta| < 2.5$ and is responsible for small im-
 131 pact parameter resolution which is important for accurate reconstruction of
 132 secondary vertices [7]. In order to produce these precise measurements a
 133 very high granularity is required. In addition to this the proximity to the

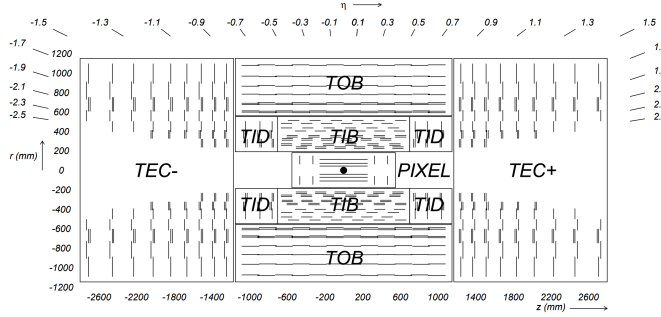


Fig. 4.3: Cross section (side) of CMS tracker prior to the Phase 1 upgrade during the year-end technical stop of 2016/2017. Each line represents a detector module while double lines indicate back-to-back strip modules. Surrounding the pixel tracker (PIXEL) is the strip detector, which is divided into the Tracker Inner Barrel (TIB), Tracker Outer Barrel (TOB), Tracker Inner Disks (TID), and Tracker Endcaps (TEC). Reprinted from Reference [6].

134 IP means that one expects there to be high occupancy of the tracker. These
135 constraints are met by using pixels with a cell size of $100 \times 150 \mu\text{m}^2$.

136 The original pixel detector was designed for operation at the nominal
137 instantaneous luminosity of $10^{34} \text{ cm}^{-2}\text{s}^{-1}$ with 25 ns between proton bunch
138 crossings, resulting in on average about 25 proton-proton interactions occur-
139 ring per bunch crossing or pileup [6]. During the LHC technical shutdown
140 of 2016/17, the pixel detector underwent the scheduled Phase 1 upgrade
141 which would allow operation at higher levels of instantaneous luminosity
142 and pileup. Figure 4.4 shows a cross sectional view in the r - z plane. Prior
143 to 2017 there were three barrel layers and two endcap layers on each side
144 which provide three very precise space points for each charged particle. The
145 upgrade decreased the radius of the innermost barrel layer from 4.4 cm to
146 3.0 cm and added a fourth barrel layer as well as adding third endcap layer
147 to each side. Each of the endcap layers consisted of two half-disks populated
148 with pixel modules whereas the upgraded endcap layers were split into inner
149 and outer rings. [5]

150 4.4.2 Strip Detector

151 The silicon strip detector surrounds the pixel detector and is comprised of
152 four subsystems, the Tracker Inner Barrel (TIB), the Tracker Outer Barrel
153 (TOB), the Tracker Inner Disks (TID), and the Tracker Endcaps (TEC),
154 all of which can be seen in Figure 4.3 [7]. The TIB and TID both use

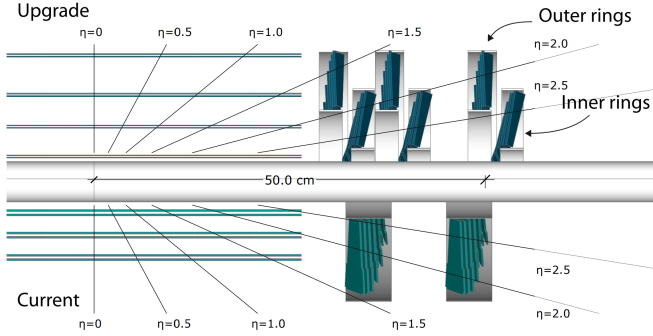


Fig. 4.4: Cross section (side) of pixel detector. The lower half , labeled "Current", shows the design prior to 2017 while the upper half, labeled "Upgrade", shows the design after the upgrade. Reprinted from Resource [5]

155 320 μm thick silicon micro-strip sensors oriented along z and r respectively.
 156 The TIB has four layers while the TID is composed of three layers. This
 157 geometry allows the TIB and TID to combine to provide up to four $r - \phi$
 158 measurements on charged particle trajectories.

159 Surrounding the TIB and TID is the TOB, which extends between $z \pm 118$
 160 cm. This subsystem consists of six layers of 500 μm thick silicon micro-strip
 161 sensors with strip pitches ranging from 122 μm to 183 μm , providing six
 162 more $r - \phi$ measurements in addition to those from the TIB/TID subsystems.
 163 Beyond the z range of the TOB is the TEC. Each TEC is made up of nine
 164 disks. Each of the nine disks has up to seven concentric rings of micro-strip
 165 sensors oriented in radial strips with those on the inner four rings being
 166 320 μm thick and the rest being 500 μm thick, providing up to nine ϕ
 167 measurements for the trajectory of a charged particle.

168 To provide additional measurements of the z coordinate in the barrel and
 169 r coordinate in the disks a second micro-strip detector module is mounted
 170 back-to-back with stereo angle 100 mrad in the first two layers of the TIB
 171 and TOB, the first two rings of the TID, and rings 1, 2, and 5 of the TEC.
 172 The resulting single point resolution is 230 μm in the TIB and 530 μm in the
 173 TOB. The layout of these subsystems ensures at least nine hits for $|\eta| < 2.4$
 174 with at least four of hits yielding a 2D measurement.

175 4.5 Electromagnetic Calorimeter

176 The electromagnetic calorimeter (ECAL) lies just outside the tracker and is a
 177 hermetic homogeneous calorimeter designed to measure the energy deposited

178 by electrons and photons. It consists of a central barrel (EB) with 61200
179 lead tungstate (PbWO_4) crystals which is closed by two endcaps (EE), each
180 having 7324 crystals. Highly-relativistic charged particles passing through a
181 crystal primarily lose energy by producing bremsstrahlung photons. Photons
182 lose energy by producing $e^- - e^+$ pairs. In front of each EE is a preshower
183 (ES) detector which acts as a two-layered sampling calorimeter. The crystals
184 in the EB are instrumented with avalanche photodiodes (APDs) while the
185 EE crystals are instrumented with vacuum phototriodes (VPTs). The ECAL
186 design was strongly driven to be sensitive to the di-photon decay channel
187 of the Higgs boson. This led to the design of a calorimeter that was fast,
188 radiation-hard, and had good spatial and energy resolution.

189 4.5.1 Crystals

190 In order to provide a good spacial resolution it was necessary for the ECAL
191 to have a fine granularity. The small Molier radius (22 mm) and short radia-
192 tion length (8.9 mm) of PbWO_4 allows for fine granularity while maintaining
193 good energy resolution by containing nearly all of the energy from an EM
194 shower without the need for a restrictively thick crystal layer. The PbWO_4
195 scintillation is also fast enough that approximately 80 percent of an EM
196 shower is produced within 25 ns, which is the also the amount of time be-
197 tween bunch crossings at the LHC. These crystals have a Gaussian-shaped
198 spectrum spanning from 360 nm to 570 nm with a maximum at approx-
199 imately 440 nm. While PbWO_4 is relatively radiation-hard, the amount
200 of ionizing radiation seen by the crystal leading up to the HL-LHC era of
201 operations causes wavelength-dependent degradation in light transmission.
202 The scintillation mechanism however is unchanged so this damage can be
203 tracked and accounted for by injecting laser light near the peak wavelength
204 of the emission spectrum into the crystals to monitor optical transparency.

205 Light produced in the crystal is transmitted along its length and col-
206 lected at the rear by either an APD in the EB or a VPT in one of the EE.
207 Light output is temperature dependent so the crystals are kept at precisely
208 18°C at which the yield is about 4.5 photoelectrons per MeV. The EB and
209 EB crystals, which have a tuncated pyramidal shape to match the lateral de-
210 velopment of the shower, along with their photosensors are shown in Figure
211 4.5.

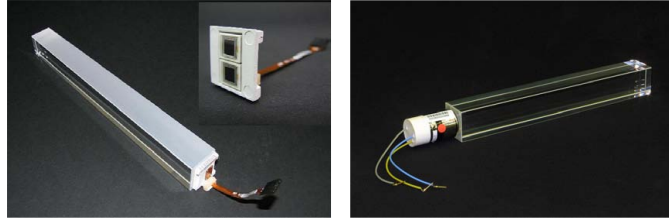


Fig. 4.5: PbWO₄ crystals. Left: EB crystal with APD. Right: EE crystal with VPT. Reprinted from [7]

212

4.5.2 Barrel and Endcaps

213 The EB covers the pseudorapidity range $|\eta| < 1.479$ and uses crystals that
 214 are 230 mm long, which corresponds to 25.8 radiation lengths. The front
 215 face of each crystal measures 22×22 mm² while the rear face measures 26×26
 216 mm². These are grouped in 36 supermodules (SM), each comprised of 1700
 217 crystals arranged in a 20×85 grid in $\phi \times \eta$. Each SM spans half the length
 218 of the barrel and covers 20° in ϕ . On the back face of each crystal is a
 219 pair of APDs (semiconductor diodes). APDs are compact, immune to the
 220 longitudinal 3.8 T magnetic field produced by the solenoid at this location,
 221 and resistant to the radiation levels expected in the EB over a ten year
 222 period. They also have high enough gain to counter to low light yield of
 223 the crystals. All of this makes them an ideal choice for use in the EB. Each
 224 APD has an active area of 5×5 mm² and are operated at a gain of 50 which
 225 requires a bias voltage between 340 and 430 V. As the gain of the APDs is
 226 highly dependent on the applied bias voltage and any gain instability would
 227 translate to degradation in energy resolution, very stable power supplies are
 228 used to maintain voltages within a few tens of mV.

229 The EE cover the pseudorapidity range $1.497 < |\eta| < 3.0$. The crystals in
 230 the EE have a 28.62×28.62 mm² front face cross section and 30×30 mm² rear
 231 face cross section. Each crystal is 220 mm long which corresponds to 24.7
 232 radiation lengths and are grouped in 5×5 units called supercrystals (SCs).
 233 Two halves, called *Dees*, make up each EE. Each Dee contains 138 SCs and
 234 18 partial SCs which lie along the inner and outer circumference. On the
 235 back of each crystal in EE is a VPT which is a conventional photomultiplier
 236 with a single gain stage. While not as compact as the APDs used in the EB,
 237 the VPTs are a more suitable for the more hostile environment at higher
 238 η . Each VPT has a 25-mm diameter and approximately 280 mm² of active
 239 area. Though the VPT gain and quantum efficiency are lower than that of
 240 the APDs this is offset by the larger active area allowing for better light

241 collection. Figure 4.6 shows the orientation of the crystals, modules, and
 242 supermodules within the ECAL. [7]

243 **4.5.3 Preshower layer**

244 In front of each EE is a preshower (ES) detector. The main purpose of the
 245 ES is to identify photons resulting from $\pi^0 \rightarrow \gamma\gamma$ within the pseudorapidity
 246 range $1.653 < |\eta| < 2.6$, but it also aids in the identification of electrons
 247 against minimum ionizing particles (MIPs) and provides a spacial resolution
 248 of 2 mm compared to the 3 mm resolution of the EB and EE. The ES acts
 249 as a two-layered sampling calorimeter. Lead radiators make up the first
 250 layer. These initiate electromagnetic showers from incoming electrons or
 251 photons. The deposited energy and transverse profiles of these showers are
 252 then measured by the silicon strip sensors which make up the second layer.

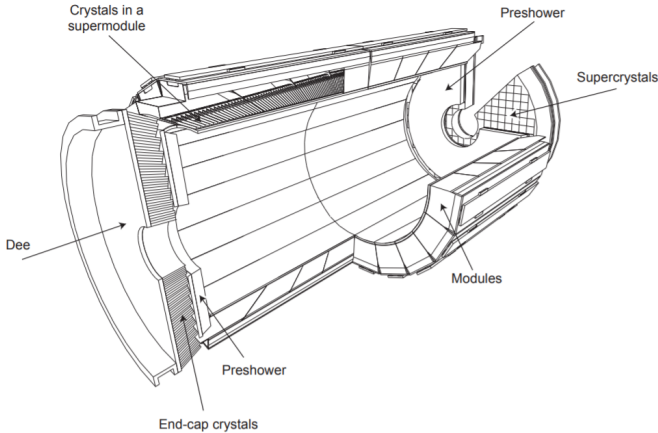


Fig. 4.6: Schematic of ECAL. Reprint from [7]

253 **4.5.4 Performance**

254 The energy resolution of the ECAL can be parameterized as

$$\frac{\sigma}{E} = \frac{S}{\sqrt{E}} \oplus \frac{N}{E} \oplus C \quad (4.4)$$

255 where S is the stochastic term characterizing the size of photostatistical
 256 fluctuations, N is the term characterizing the contributions of electronic,
 257 digital, and pileup noise, and C is a constant which accounts for crystal

258 performance non-uniformity, intercalibration errors, and leakage of energy
 259 from the back of a crystal. The values for these terms, as measured in a
 260 beam test using 20 to 250 GeV electrons, are $S = 0.028 \text{ GeV}^{1/2}$, $N = 0.12$
 261 GeV, and $C = 0.003$. [7]

4.6 Hadronic Calorimeter

263 In the space between the bore of the superconducting magnet and the ECAL
264 is the Hadronic Calorimeter (HCAL). The HCAL is a sampling calorimeter
265 used for the measurement of hadronic jets and apparent missing transverse
266 energy resulting from neutrinos or exotic particles. A longitudinal cross-
267 section of the HCAL is shown in Figure 4.7.

268 Need to fix the citation for this figure

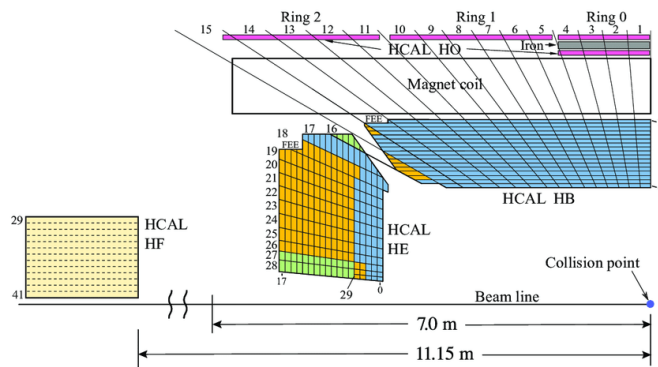


Fig. 4.7: Longitudinal view of HCAL

4.7 Muon System

270

5. MIP TIMING DETECTOR (MTD)

271

5.1 Introduction

272 In the coming years the LHC will be working toward upgrades that will
 273 lead a substantial increase in luminosity. The timeline for future operations
 274 of the LHC is shown in Figure 5.1. In 2019 the LHC entered a two-year
 275 shutdown, Long Shutdown 2 (LS2). Upgrades of the LHC injector complex
 276 to increase the beam brightness will take place during this shutdown. After
 277 LS2 the LHC will enter Run 3 which will run for three years at 13-14 TeV. At
 278 the completion of Run 3 the LHC will enter Long Shutdown 3 (LS3) which
 279 will last approximately 2.5 years. During LS3 the optics in the interaction
 280 region will be upgraded to produce smaller beams at the interaction point.
 281 The completion of this upgrade will usher in the High Luminosity (HL-LHC)
 282 era or Phase 2 of LHC operations, during which the combination of brighter
 283 beams and a new focusing scheme at the IP allows for a potential luminosity
 284 of $2 \times 10^{35} \text{ cm}^{-2}\text{s}^{-1}$ at the beginning of each fill [1].

LHC/ High-Luminosity LHC timeline

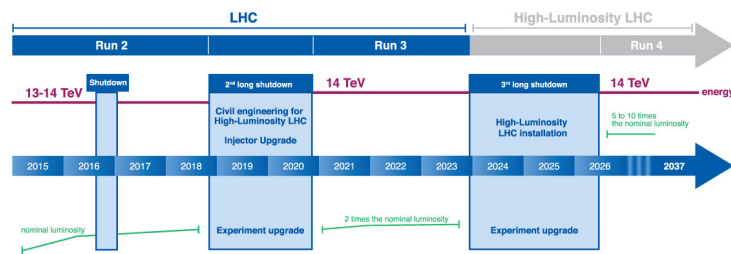


Fig. 5.1: Timeline for LHC [8]

285

The increased luminosity results in more interactions per bunch crossing or pileup. In order to limit the amount of pileup the experiments must

disentangle to more manageable levels, the nominal scenario would be operating at a stable luminosity of $5.0 \times 10^{34} \text{ cm}^{-2} \text{ s}^{-1}$. This would limit the pileup to an average of 140. The ultimate scenario for operations would be running at $7.5 \times 10^{34} \text{ cm}^{-2} \text{ s}^{-1}$ which brings the average pileup up to 200. The CMS detector in its current state is not capable of dealing with $\approx 140\text{-}200$ pileup. At this level of pileup the spacial overlaps of tracks and energy depositions would lead to a degradation in the ability to identify and reconstruct hard interactions. In order to preserve the data quality of the current CMS detector this increased pileup must be reduced to an equivalent level approximately equal to current LHC operations which is ~ 40 . The collision vertices within a bunch crossing have an RMS spread of 180-200 ps in time. If the beam spot were to be sliced into consecutive snap shots of 30-40 ps then the pileup levels per snapshot would be approximately 40. The space-time reconstruction of a 200 pileup event is shown in Figure 5.2. The addition of timing information to the z position spreads apart the vertices that would otherwise have been merged together and indiscernible. In order to achieve this a detector dedicated to the precise timing of minimum ionizing particles (MIPs), the MTD, will be added to the CMS detector.

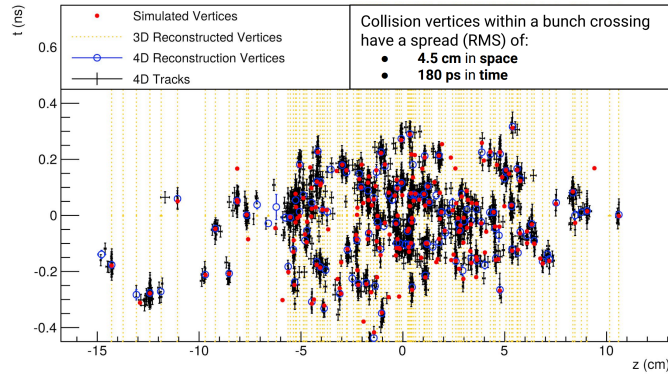


Fig. 5.2: Vertices from a simulated 200 pileup event. Need to replace this with the figure from the TDR.

BIBLIOGRAPHY

- [1] G. Apollinari, O. Brüning, T. Nakamoto, and Lucio Rossi. High Luminosity Large Hadron Collider HL-LHC. *CERN Yellow Rep.*, (5):1–19, 2015.
- [2] S Baird. Accelerators for pedestrians; rev. version. Technical Report AB-Note-2007-014. CERN-AB-Note-2007-014. PS-OP-Note-95-17-Rev-2. CERN-PS-OP-Note-95-17-Rev-2, CERN, Geneva, Feb 2007.
- [3] David Barney. CMS Slice. Feb 2015.
- [4] Jean-Luc Caron. Cross section of lhc dipole.. dipole lhc: coupe transversale. ”AC Collection. Legacy of AC. Pictures from 1992 to 2002.”, May 1998.
- [5] CMS Collaboration. CMS Technical Design Report for the Pixel Detector Upgrade. Technical Report CERN-LHCC-2012-016. CMS-TDR-11, Sep 2012. Additional contacts: Jeffrey Spalding, Fermilab, Jeffrey.Spalding@cern.ch Didier Contardo, Universite Claude Bernard-Lyon I, didier.claude.contardo@cern.ch.
- [6] CMS Collaboration. Description and performance of track and primary-vertex reconstruction with the CMS tracker. *JINST*, 9(CMS-TRK-11-001. CERN-PH-EP-2014-070. CMS-TRK-11-001):P10009. 80 p, May 2014. Comments: Replaced with published version. Added journal reference and DOI.
- [7] The CMS Collaboration. The CMS experiment at the CERN LHC. *Journal of Instrumentation*, 3(08):S08004–S08004, aug 2008.
- [8] Cinzia De Melis. Timeline for the LHC and High-Luminosity LHC. Frise chronologique du LHC et du LHC haute luminosité. Oct 2015. General Photo.
- [9] Lyndon Evans and Philip Bryant. LHC machine. *Journal of Instrumentation*, 3(08):S08001–S08001, aug 2008.

- [10] Tai Sakuma and Thomas McCauley. Detector and event visualization with SketchUp at the CMS experiment. *Journal of Physics: Conference Series*, 513(2):022032, jun 2014.